Mechanical model of blebbing in nuclear lamin meshworks

Chloe M. Funkhouser[a], Rastko Sknepnek[a], Takeshi Shimi[b], Anne E. Goldman[b], Robert D. Goldman[b], and Monica Olvera de la Cruz[a,c,1]

Departments of [a]Materials Science and Engineering and [c]Chemistry, Northwestern University, Evanston, IL 60208; and [b]Department of Cell and Molecular Biology, Feinberg School of Medicine, Northwestern University, Chicago, IL 60611

Contributed by Monica Olvera de la Cruz, January 7, 2013 (sent for review November 26, 2012)

Much of the structural stability of the nucleus comes from meshworks of intermediate filament proteins known as lamins forming the inner layer of the nuclear envelope called the nuclear lamina. These lamin meshworks additionally play a role in gene expression. Abnormalities in nuclear shape are associated with a variety of pathologies, including some forms of cancer and Hutchinson–Gilford Progeria Syndrome, and often include protruding structures termed nuclear blebs. These nuclear blebs are thought to be related to pathological gene expression; however, little is known about how and why blebs form. We have developed a minimal continuum elastic model of a lamin meshwork that we use to investigate which aspects of the meshwork could be responsible for bleb formation. Mammalian lamin meshworks consist of two types of lamin proteins, A type and B type, and it has been reported that nuclear blebs are enriched in A-type lamins. Our model treats each lamin type separately and thus, can assign them different properties. Nuclear blebs have been reported to be located in regions where the fibers in the lamin meshwork have a greater separation, and we find that this greater separation of fibers is an essential characteristic for generating nuclear blebs. The model produces structures with comparable morphologies and distributions of lamin types as real pathological nuclei. Thus, preventing this opening of the meshwork could be a route to prevent bleb formation, which could be used as a potential therapy for the pathologies associated with nuclear blebs.

elasticity | Monte Carlo | simulation

The nuclear lamina is a component of the nuclear envelope, whose major structural element is a mesh of type V intermediate filament proteins called lamins. It is the most interior component of the nuclear envelope, located underneath the inner nuclear membrane. There are four major kinds of lamins, which can be split into two types, A and B types. Lamins A and C are A type and encoded by the same gene, whereas lamins B1 and B2 are B type but coded by different genes. Lamins are present at the periphery of the nucleus, where they form the nuclear lamina, but both A- and B-type lamins are also found throughout the nucleoplasm in a relatively nonstructured form with a much higher mobility compared with those lamins incorporated into the lamina meshworks. It has been reported that the nuclear lamina contributes to the mechanical stability of the nucleus (1–3). Lamins have also been found to interact with chromatin and thus, can affect gene expression and DNA replication (4–6).

Changes in the overall 3D shape of the nucleus are indicative of a variety of pathologies. Many of these pathologies are the result of mutations in the genes coding for lamins A/C, termed laminopathies (7–9). Examples of such pathologies include the premature aging disorder Hutchinson–Gilford Progeria Syndrome (progeria), Emery–Dreifuss muscular dystrophy, dilated cardiomyopathy, and generalized lipodystrophy. Additionally, multiple forms of cancer are associated with misshapen nuclei (10). Often, the changes in the overall nuclear shape include the formation of structures called nuclear blebs, defined as protrusions from the nuclear surface (8). In progeria, for example, a blebbed region of the lamina tends to be composed of mostly A-type lamins, largely excluding B-type lamins (11). Another potentially important characteristic of nuclear blebs is that the local lamin meshwork tends to have a larger mesh size, meaning that there is a greater spacing between lamin fibers compared with the rest of the nucleus or a nonblebbed nucleus (12–16), which is shown in Fig. 1*A*. The causes of the formation of nuclear blebs are unknown and may be related to the pathology of the associated diseases, such that new therapies could potentially be targeted to the underlying cause of the blebs.

Mechanical studies of the nuclear lamina have been conducted [as reviewed, for example, by Rowat et al. (17)], including the use of micropipette aspiration (1, 2, 18) and atomic force microscopy (19) to extract mechanical properties. A limited number of computational studies of the nuclear lamina have also been carried out, including one using finite-element methods to examine the response to imposed deformation in an axisymmetric model (20). The mechanics of crack propagation in a regular meshwork representing the *Xenopus* nuclear lamin meshwork have been examined (21), whereas the retraction of artificially induced blebs has been modeled by Wren et al. (22), treating the lamin meshwork as a network of Hookean springs. The lamin meshwork has also been modeled as a 2D elastic solid in attempts to provide an explanation for results obtained by aspiration with micropipettes (2). These studies have examined the mechanical response of the entire nuclear lamina to particular kinds of externally applied deformation or on a smaller scale, as in the study of crack propagation.

In this study, we examine how the material properties of the lamin meshwork could alone lead to the formation of blebs in the absence of external stimuli. A simple mechanical model is used to describe the morphology of a nuclear lamin meshwork along with the arrangement of the lamin components. The meshwork is treated as a two-component thin elastic shell with spherical topology. We explore which mechanisms may be responsible for the formation of nuclear blebs as well as the segregation of lamin isoforms within blebs. We modify a model for multicomponent elastic membranes (23) to describe nuclear lamin meshworks. We note that blebbing is not limited to the cell nucleus but plays a central role in cell spreading and retraction (24). We propose here a different mechanism for the formation of nuclear blebs.

Results and Discussion

The model developed here applies to mammalian nuclei, which as opposed to the often-pictured *Xenopus* oocyte nuclei (25), have a more randomly oriented, less-ordered meshwork (26, 27). This less-ordered meshwork can, thus, be modeled as an isotropic material. The thickness of the nuclear lamin meshwork has been reported (28–30) as $h \sim 10$–80 nm, and attachments with chromatin within the nucleus may result in a slight increase in the

Author contributions: C.M.F., R.S., R.D.G., and M.O.d.l.C. designed research; C.M.F., R.S., T.S., and A.E.G. performed research; C.M.F., R.S., T.S., A.E.G., and M.O.d.l.C. analyzed data; and C.M.F., R.S., R.D.G., and M.O.d.l.C. wrote the paper.

The authors declare no conflict of interest.

[1]To whom correspondence should be addressed. E-mail: m-olvera@northwestern.edu.

This article contains supporting information online at www.pnas.org/lookup/suppl/doi:10.1073/pnas.1300215110/-/DCSupplemental.

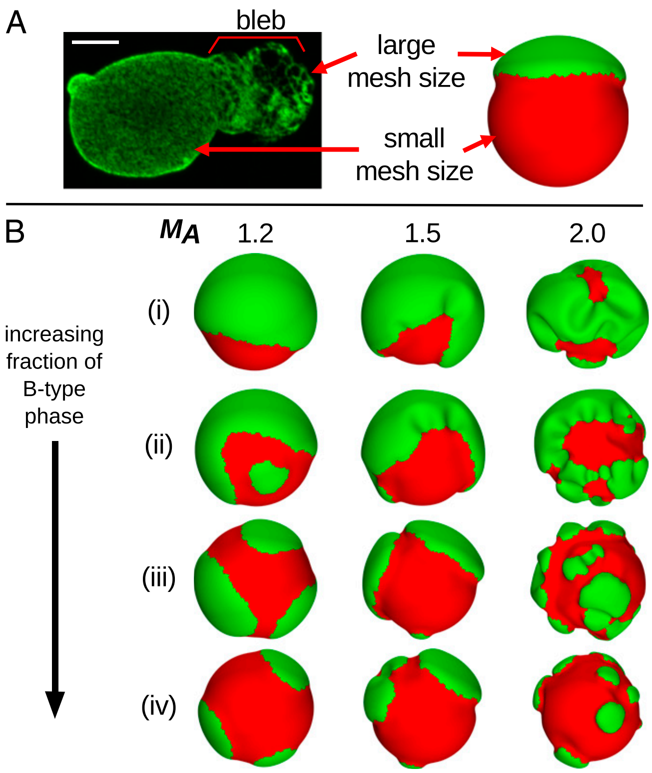

Fig. 1. Relating mesh size in (*A*) experimental and simulation structures along with (*B*) simulation results for different parameters. (*A*) Nucleus from a breast cancer cell with lamin A stained, showing a larger mesh size in the bleb compared with the rest of the nucleus. (Scale bar: 5 μm.) The A-type component in the simulations (green) is analogously assigned to have a larger mesh size than the B-type component (red). (*B*) Low-energy configurations for lamin meshwork systems with phase fractions of the red B-type component of (*i*) $f = 0.2$, (*ii*) $f = 0.4$, (*iii*) $f = 0.6$, and (*iv*) $f = 0.8$. From left to right, the columns show systems with mesh size area scaling factors of M_A = 1.2, 1.5, and 2.0, respectively, corresponding to the A-type component preferring a mesh size that is 20%, 50%, or 100% larger than the initial sphere, respectively. For clarity, dual meshes are shown here rather than vertices.

effective thickness that could affect the mechanical properties of the meshwork. However, we treat the lamin meshwork as a thin shell, because it has been shown that the elastic properties of the nucleus originate largely from the lamin meshwork rather than the interior contents (1); also, the effective thickness of the meshwork is much smaller than the lateral dimensions ($R \sim 10$ μm), with a thickness-to-size ratio $h/R \sim 10^{-3}$–10^{-2}. Experiments employing fluorescence recovery after photobleaching (FRAP) techniques have revealed that lamins within the lamina meshwork are relatively stable over time (31, 32), and therefore, the meshwork is treated as a solid rather than a liquid structure. Based on the results of a study showing that the lamina returns to its original shape when deformed mechanically (1), we assume in this study that the lamin meshwork has an elastic character. The mechanical behavior of the lamin meshwork may present some viscoelastic character with a time-dependent elastic response (33, 34), possibly as a result of dynamic polymerization or reorganization of the lamin filaments. However, in this study, we concentrate on stable shapes of the meshwork and thus, ignore such effects, treating it as an elastic material as a first approximation. Lastly, the model assumes that the lamin meshwork is fully intact as in interphase and does not address assembly or disassembly of the meshwork. Therefore, it is justifiable to model the nuclear lamin meshwork as an isotropic 2D solid elastic shell with spherical topology.

It has been reported that A- and B-type lamins form separate but interacting meshworks (16, 26), although the details of the interactions between the different lamin types are unclear. Therefore, for simplicity, lamin components are grouped into A- and B-type lamins, such that the meshwork is described as having two components rather than four, because the lamins within each type are structurally similar. In the model, we specify that each spatial point on the meshwork surface can be occupied by only a single component. Because even highly segregated regions of lamin meshworks likely still contain small amounts of the excluded lamin type, a spatial point of our component A represents a phase that is rich in A-type lamins, and a point of our component B represents a phase that is rich in B-type lamins, with each phase having its own distinct mechanical properties.

We use a continuum approach to model the nuclear lamin meshwork at mesoscopic scales, such that details at the level of individual lamin fibers are not represented but rather, averaged over. The total elastic energy of a thin shell can be written as a sum of stretching and bending energies (35), with their relative contributions determined by the dimensionless ratio $(R/h)^2$ (36). We describe the mechanics of the lamin meshwork in terms of a competition between 2D stretching energy and bending energy defined with respect to a reference state. The contributions to the stretching and bending energies can be written separately for each of the two components, allowing for the flexibility to assign different mechanical properties to each component. These mechanical properties include the Young's modulus ($Y_{A,B}$), thickness ($h_{A,B}$), Poisson's ratio ($\nu_{A,B}$), bending modulus ($\kappa_{A,B}$), and spontaneous or preferred curvature ($H^{(0)}_{A,B}$).

The reference state, described in terms of the component-specific reference metric tensor $\hat{g}_{A,B}$ (37), is the configuration that each component would prefer to take (that is, it has both stretching and bending energies equal to zero). We take the reference state to be a sphere, where the radius, $R^{(0)}_{A,B} = 1/H^{(0)}_{A,B}$, can be adjusted to reflect particular properties of the meshwork components. An observation that has been made in many blebbed nuclei associated with a variety of pathologies is that the meshwork in the bleb, frequently rich in A-type lamins, has a larger mesh size than the B type-rich regions or any meshwork that has been described to date in a normal nucleus, which is shown in Fig. 1*A* (12–16). This tendency to form an enlarged meshwork can be represented in this model by scaling the reference metric tensor of one of the components by a positive constant mesh area scaling factor, $M_{A,B}$ [e.g., $\hat{g}_A \rightarrow (M_A)\hat{g}_A$ and $(R^{(0)}_A)^2 \rightarrow M_A(R^{(0)}_A)^2$]. Applying $M_{A,B}$ to the reference state specifies that regions occupied by that component will prefer to increase their surface area from the initial state, because the reference state now describes a larger sphere. This increase in surface area mimics a constant number of lamin fibers forming a meshwork with larger mesh size, thus occupying more area than a meshwork of the same number of fibers but with a smaller mesh size.

We perform a series of simulations to explore parameter space to determine which meshwork properties may be responsible for nuclear blebbing, focusing on how differences in preferred mesh size, thickness, and the fraction of the two components affect the low-energy stable shapes formed by the meshwork. For simplicity, the B-type component is always set to have a mesh area scaling factor of $M_B = 1$, meaning that there is no natural tendency for changes in its mesh size, whereas the A-type component is set to have M_A = 1.2, 1.5, or 2.0. M_A = 1.2 corresponds to the A-type component preferring to increase in surface area (and mesh size) by 20% compared with the initial state or the B-type component. The fraction of meshwork occupied by the B-type component is varied between f = 0.2 and 0.8. It has been reported that A-type lamins have a larger diameter than B-type lamins and that the lamina is thicker in regions with A-type lamins (26). Additionally, in progeria, the premature aging disease of children, a mutant form of lamin A known as progerin has been found to abnormally accumulate at the lamina (11), which could also contribute to a thicker lamina in A-type regions. Lastly, A-type lamins seem to contribute to the mechanical rigidity and stiffness of the lamina more than B-type lamins (3, 19, 26). To investigate how these reported differences in the properties of A-type and B-type lamins could affect nuclear morphologies, we have specified that, in A-type regions, the thickness of the lamin meshwork is two times the thickness of B-type regions, $h_A = 2h_B$. Because the 2D Young's modulus $Y \propto h$ and bending modulus $\kappa \propto h^3$ (38), the A-type regions have a Young's modulus that is two times larger and a bending modulus that is eight times larger than the B-type regions. We note that, although Y, κ, and h are interrelated, we do not relate these parameters to the mesh area scaling factor M, because the specific parameters of lamin meshworks required to formulate such a relation have not been reported.

Fig. 1*B* presents results across a range of component fractions and mesh area scaling factors. We observe that the components segregate as a result of the differences in one or more of the mechanical properties (M, Y, or κ); we emphasize that there is no additional penalty imposed for mixing. It has been shown that, in multicomponent elastic membranes, segregation of membrane components can arise, even in the absence of a mixing penalty, when the components have disparate bending rigidities (23, 39). To determine more precisely the cause of the segregation observed here, we have performed simulations where the components have equal elastic parameters h, Y, and κ, such that their only difference is in the preferred mesh size M (Fig. S1). Those results exhibit a similar segregation as these results, even with the smallest value of scaling factor M_A used. Lastly, for simulations where there is no difference in preferred mesh size between the components (i.e., $M_A = M_B = 1$) but the A-type component is two times as thick as the B-type component, no significant degree of segregation is observed (Fig. S2). We, thus, conclude that the difference in preferred mesh size, modeling the expansion of the A-type component only, is essential to produce a compositionally segregated system.

Contrasting the morphologies presented in Fig. 1*B*, it is clear that, for greater mesh area discrepancies between components (i.e., larger values of M_A), deformations from a spherical morphology are more extreme. Thus, for nuclear bleb-like structures to form, the expansion of the meshwork in regions rich in A-type lamins must be significant, because we find that it must be on the order of a twofold expansion in terms of area. Additionally, when the fraction of the B-type component is more than 0.5 ($f > 0.5$), the morphologies more closely resemble the morphologies of experimental images, where the expanding A type-rich regions form isolated protruding structures, such as in the systems in Fig. 2 *A*–*C*.

For systems with $M_A = 1.5$ and 2, the meshwork in the A-type regions exhibits a wrinkled structure, particularly when $f < 0.5$, with folds along the boundaries as opposed to the largely smooth cap-like structures for $f > 0.5$. This wrinkling originates from the constraints on the boundaries of the A-type regions imposed by the B-type regions, because the meshwork as a whole is forced to form a closed surface. This type of wrinkling resulting from an expanding yet constrained meshwork could be responsible for the experimentally observed distribution of A- and B-type regions and thus, the clefts between adjacent lobules in highly deformed nuclei, such as in Fig. 2 *E* and *F*. We note that similar phenomena have been reported in the curling of constrained elastomeric bistrips (40), where components are glued together and one prefers to contract while the other is unstrained. Wrinkling of bodies with heterogeneous swelling has been studied in the context of plant leaf tissue growth and torn plastic sheets (41–43), where imposing prescribed reference metrics produces wavy or wrinkled structures; however, because these systems have a free edge that is able to deform out of the plane, the wrinkles form a fractal-like cascade, where only the larger wavelengths seem similar to the wrinkling that we observe. The use of reference metrics to model differential swelling has been reviewed by Sharon and Efrati (44).

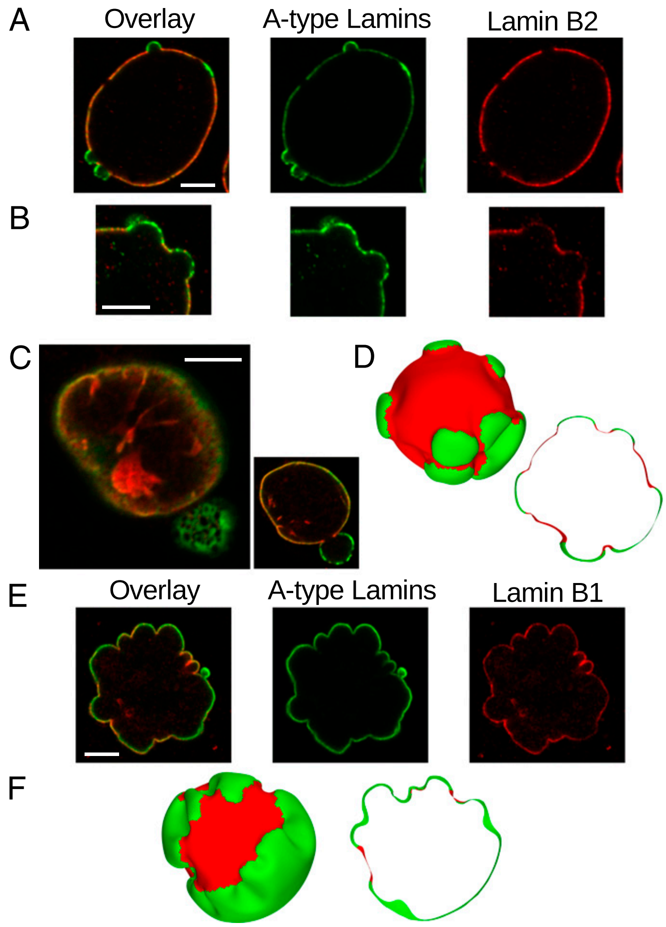

Fig. 2. Comparisons between simulation results and experimental images of nuclear lamin meshworks. In all images, A-type lamins are shown in green, and B-type lamins are shown in red (using fluorescent tags in experimental images); Overlay images superimpose the fluorescence from both lamin types. (*A* and *B*) Blebbed nuclei of HeLa cells with lamin B1 silenced shown in the cross-section, with deformation and segregation of lamin types similar to the simulation result in *D*, where blebs appear as protrusions rich in A-type lamins. (*C*) A blebbed nucleus of a breast cancer cell where the mesh size is clearly larger in the blebbed region compared with the main body of the nucleus (shown as an overlay of both lamin types). The larger image shows a plane close to the surface to reveal the mesh size, whereas the smaller image shows a cross-section approximately through the midplane. Lamin B1 is stained in red. (*D*) Simulation result with $M_A = 2.0$ and $f = 0.8$ showing the surface and a cross-section. (*E*) Highly lobulated nucleus from a fibroblast of a progeria patient with the E145K-LA mutation, showing a lesser degree of segregation than the nuclei in *A*–*C* but still exhibiting a higher concentration of B-type lamin between the lobules. (*F*) Simulation result with $M_A = 2.0$ and $f = 0.4$ showing the surface and a cross-section resembling the lobulated structure in *E*. (Scale bars: 5 μm.) [*A* reprinted with permission from ref. 16 (Copyright 2008, Cold Spring Harbor Laboratory Press).]

The process of nuclear blebbing, as described by our simple continuum model, is rather general. It can be thought of as follows. Given a two-phase surface, where one phase prefers to expand, deformations such as wrinkles or bleb-like protrusions will form, because the phases are subject to constraints. We find that whether we observe blebs or wrinkles is dependent on the phase fraction f. We note that wrinkling of closed shells with elastic heterogeneities was successfully described by a recent related continuum model (45). In nuclear lamin meshworks, the underlying processes leading to lamin mobility and mesh size expansion are complex; however, we are able to reproduce the overall nuclear morphologies by describing the system as having two phases with different expansion tendencies.

Two very different time scales determine the morphology of the meshwork. The short time scale corresponds to a fast relaxation of the local conformation, whereas the long time scale is associated with a much slower rearrangement of the components, perhaps on the order of hours. Lamin mobility seems to be achieved by an exchange of lamins between the lamina and nucleoplasm. However, little has been reported regarding the dynamics of the process of nuclear bleb formation. Although the simulations do not properly model dynamics, the effective mobility of the lamins can be qualitatively controlled by tuning the simulated annealing cooling rate for swapping, which is a simulation parameter related to how easily the components can rearrange. Below a certain temperature (dependent on the specific system parameters), the component distribution is quenched, and only the shape is relaxed. In this sense, the structures that we obtain should not be understood as global minima of the elastic energy but morphologies corresponding to the local minima for a given distribution of A- and B-type lamins. By tuning the cooling rate, we find that the effective mobility of the lamin components impacts the sizes of the blebs produced. For fast cooling, the components are more restricted, less segregation occurs before deformation, and thus, numerous smaller blebs are formed; when components are less restricted, fewer larger blebs form. The results from varying the cooling rate are presented in Fig. 3, illustrating the different number and sizes of blebs produced. Indeed, experimentally, nuclear blebs tend to appear in a variety of sizes and morphologies, and this variation may be related to the degree to which the lamin types exchange with the nucleoplasm compared with the deformation induced by the mesh size expansion.

Fig. 4 presents plots of bending energy, stretching energy, and mean curvature on the surface of meshwork systems with small deformations (Fig. 4*A*) and larger deformations (Fig. 4*B*). In both systems, the stretching energy concentrates at the interfaces between segregated single-component regions, where it is more difficult for each component to adopt its preferred mesh size, because they must remain connected. The bending energy is similar, although it has its maximum in a negative-curvature region between two bleb-like structures that formed but failed to disconnect. For both the bending and stretching energies, the minimum and maximum values are one order of magnitude larger for the system with $M_A = 1.5$ compared with the system with $M_A = 1.2$, emphasizing the importance of this preferred mesh size parameter.

Some of the simplifying assumptions made in this model exclude aspects of the system that may be additionally involved in nuclear bleb formation and will be addressed in future studies. One such extension is to model the meshwork as a viscoelastic material and examine the time scales of the bleb-forming process along with the segregation of lamin components. This investigation may lead to answers as to why different blebs remain stable at different sizes and why their coarsening often seems arrested. The chromatin contained within the nucleus is known to associate with the inner surface of the lamina (e.g., through lamin-associated proteins) and contributes to the mechanical response of the nucleus as a whole; thus, chromatin may be important for nuclear bleb formation. Lamin-associated proteins also form connections between the lamina and the inner nuclear membrane in addition to nuclear pore complexes spanning both nuclear membranes and the lamina. These associations with the nuclear membrane(s) could impose additional mechanical effects. Physical connections to the cytoskeleton through the linker of nucleoskeleton and cytoskeleton (LINC) complex (reviewed in refs. 46–48) may also relate to nuclear blebbing as part of the mechanotransduction pathway from the cell exterior to the nucleus (49).

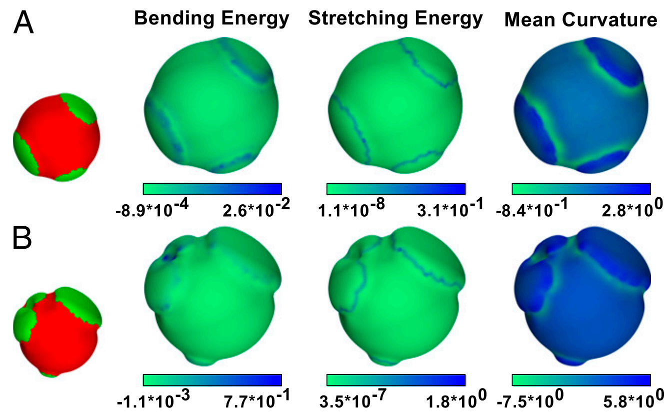

Fig. 4. Bending and stretching energies per vertex in units of κ_B with mean curvature per vertex in units of $1/R_0$. The composition is shown in the small figures on the left for reference. The system in *A* has $M_A = 1.2$ and $f = 0.8$, whereas the system in *B* has $M_A = 1.5$ and $f = 0.8$, exhibiting larger deformations, where the difference between the minimum and maximum radii in *B* is approximately two times as large as in *A*.

To conclude, we find that the enlarged mesh size of the regions rich in A-type lamins, in contrast to the normal (smaller) mesh size of the regions rich in B-type lamins, is sufficient to not only cause segregation of the lamin components but also to form nuclear blebs. We impose no penalty for mixing of the components, such as a line tension, and thus, the observed segregation of the lamin components is solely a result of their mechanical properties. We also have determined that the difference in mesh size is the required characteristic for segregation rather than differences in elastic and bending moduli. Although line tension is known to produce segregation in multicomponent elastic systems (50), it does not seem to be necessary in the lamin meshwork system that we study here. The greater the discrepancy in mesh size, the more deformation is observed, and lastly, we find that the ability of the lamin components to rearrange affects the size of the blebs.

Our results suggest that, if the enlargement of the mesh can be reduced or prevented, there will be fewer or no nuclear blebs formed. Understanding the mechanical and structural mechanisms responsible for nuclear bleb formation should provide new insights into novel targets for drug intervention in the many diseases caused by mutations in lamin A (16).

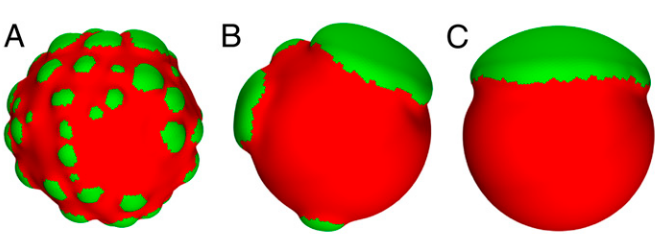

Fig. 3. Comparisons of component relaxation cooling rates, related to how easily the A- and B-type components may rearrange during the simulation, for a system with $M_A = 1.5$ and $f = 0.8$. From *A* to *C*, the restriction is eased (i.e., the components may more easily be rearranged), and the number of blebs decreases, whereas their sizes increase.

Materials and Methods

Theory and Simulations. We model the nuclear lamin meshwork within the continuum theory of thin elastic shells with the elastic energy given as a sum of stretching and bending energies, $E = E_s + E_b$ (38, 45, 51),

$$E_s = \frac{E}{2(1-\nu^2)} \int h(\vec{r}) \left(\nu (\mathrm{Tr}\,\hat{u})^2 + (1-\nu)\mathrm{Tr}(\hat{u}^2) \right) dA \quad [1]$$

and

$$E_b = \frac{E}{12(1-\nu^2)} \int h^3(\vec{r}) \left(2(H - H_0(\vec{r}))^2 - (1-\nu)(K - 2H\, H_0(\vec{r}) + K_0(\vec{r})) \right) dA, \quad [2]$$

where $\hat{u}$ is the 2D strain tensor with components (52) $u_{\alpha\beta} = \frac{1}{2}(G_{\alpha\beta} - g_{\alpha\beta}) = \frac{1}{2}(D_\alpha\, u_\beta + D_\beta\, u_\alpha + D_\alpha\, u_\gamma D_\beta\, u_\gamma)$. $G_{\alpha\beta}$ is the component of the metric tensor of the deformed shell, D_α is the covariant derivative in the direction of the tangent vector $\vec{e}_\alpha$ (with respect to the reference metric tensor components $g_{\alpha\beta}$), and u_α ($\alpha = 1, 2$) are components of the displacement vector. Tr denotes the trace, E is the 3D Young's modulus, $h(\vec{r})$ is the position-dependent thickness of the shell, ν is Poisson's ratio, $dA = \sqrt{|\hat{g}|}dx_1\, dx_2$ is the area element on the surface, where $|\hat{g}|$ is the determinant of the reference metric tensor, H is the mean curvature, and K is the Gaussian curvature. The mean and Gaussian curvatures are related to principle radii of curvature, R_1 and R_2, because $H = \frac{1}{2}\left(\frac{1}{R_1} + \frac{1}{R_2}\right)$ and $K = 1/(R_1\, R_2)$, respectively. Finally, $H_0(\vec{r}) = 1/R_0(\vec{r})$ and $K_0(\vec{r}) = 1/(R_0(\vec{r}))^2$ are reference (spontaneous) mean and Gaussian curvatures given in terms of the position-dependent radius R_0 of the reference spherical configuration. A derivation of Eq. 2 can be found in *SI Text*.

Obtaining optimal shell shapes involves minimizing the total elastic energy, which is analytically intractable for a general multicomponent system with arbitrary geometry. Instead, we use a discretized version of the elastic energy and numerical methods to obtain optimal shapes. The shell is represented as a discrete surface in 3D space created by distributing vertices randomly (but evenly) over the surface. Even distribution of vertices is achieved by performing a Monte Carlo simulation of particles of diameter σ confined to move on the surface of a sphere and interacting through the Weeks–Chandler–Andersen potential (53). The surface is constructed using the STRIPACK algorithm (54) for Delaunay triangulation on a sphere. Because we are assuming that lamin meshworks are an elastic medium, connectivity of the discrete triangulation is kept fixed. The components are defined with respect to vertices, such that each vertex represents either an A- or B-type component, with each initial configuration having a uniform random distribution of the component types. Results were reproduced for structures with approximately $N_v = 1.2 \times 10^4$ vertices, with mesh refinement during the minimization procedure. We note that the vertices in the discrete model do not represent actual lamin molecules or filaments, but they describe regions of the lamin meshwork large enough to render the continuum description valid but small enough so that any variations in the mechanical properties within the region can be neglected.

The discrete stretching energy is defined by assigning a harmonic spring to each edge connecting vertices (36, 55):

$$\tilde{E}_s = \frac{\epsilon_{t(i)}}{2} \sum_{i=1}^{N_e} \left(l_i - c_{t(i)} l_i^0\right)^2, \qquad [3]$$

where the sum is carried over all edges N_e, $\epsilon_{t(i)}$ is the spring constant, with the subscript $t(i)$ being the type of the ith vertex (A or B), l_i is the length of the ith edge, and l_i^0 is its unstretched length determined for each edge from the initial spherical configuration to construct a reference state with zero stretching energy. The spring constant is related to the 2D Young's modulus (56) as $\epsilon = \sqrt{3}Y/2$ with $\nu = 1/3$. The scaling factor $c_{t(i)}$ is introduced to model the preferred mesh size of each component. We note that the scaling factor $c_{t(i)}$ is the square root of the mesh area scaling factor $M_{t(i)}$, because $c_{t(i)}$ is associated with edges (1D entities) rather than triangles (2D objects).

The discrete bending energy, $\tilde{E}_b$, is computed as a sum over all vertices, N_v, as

$$\tilde{E}_b = \frac{E}{12(1-\nu^2)} \sum_i^{N_v} A_i \left(h_{t(i)}\right)^3 \left(2\left(H_i - H_{t(i)}^{(0)}\right)^2 - (1-\nu)\left(K_i - 2H_i\, H_{t(i)}^{(0)} + K_{t(i)}^{(0)}\right)\right), \qquad [4]$$

where A_i is the area element associated with each vertex computed as $A_i = \sum_T A_T/3$, with A_T being the area of a triangle belonging to the star of vertex i and the sum is carried over all triangles in the star. Component-specific spontaneous mean and Gaussian curvatures are defined as $H_{t(i)}^{(0)} = 1/R_{t(i)}^{(0)} = 1/(c_{t(i)}\, R_0)$ and $K_{t(i)}^{(0)} = 1/(R_{t(i)}^{(0)})^2 = 1/(c_{t(i)}\, R_0)^2$, respectively. The length scale ℓ is set by the initial system size as $R_0 = 10\ell$, such that $\ell = 1$ in the simulation approximately corresponds to 1 μm. The energy scale is set by the bending modulus of the B-type component as $\kappa_B = Eh_B/(12(1-\nu^2)) = 1$. We take the thickness to be $h_B = 0.2\ell$, such that $h/R = 2 \times 10^{-2}$, which is reasonably close to the thickness to size ratio in a typical nucleus, as discussed in the introduction. The 3D Young's modulus of the nucleus, $E = Yh$, has been reported as ∼1 kPa (18), and thus, we calculate the spring constant in Eq. **3** to be $\epsilon \sim 230\ \kappa_B/\ell^2$.

The discrete mean curvature at vertex i is computed as a sum over all edges in the vertex star (57) as $H_i = (\sum_j l_j \beta_j)/(4A_i)$, where β_j is the angle between the normals of the two triangles sharing that edge. Gaussian curvature at vertex i is computed (57) as $K_i = (2\pi - \sum_j \theta_j)/A_i$, where θ_j is the angle at the vertex of the jth triangle and the sum is carried over all triangles in the star. We note that there are numerous alternative ways to construct expressions for the discrete mean curvature and thus, the discrete bending energy (36, 56, 58, 59). The expression used in this study can be implemented efficiently and does not suffer from problems associated with irregular triangulations (58). We also point out that the associated vertex area is often computed as the area of a dual lattice cell (60), with the vertex being in its center. In the case of a Delaunay triangulation, this area is a Voronoi cell of the vertex. We have performed a series of tests that show that, within the accuracy of our simulations, the optimal shapes are insensitive to the choice of the expression for the discrete bending energy or the precise definition of the associated vertex area. Finally, to prevent unphysical self-intersections of the triangulated surface, we include a hard-core repulsion between all vertices, imposed when the Euclidean distance between two arbitrary vertices is less than their diameter, σ, chosen to be compatible with the distribution of the unstretched edge lengths.

A Monte Carlo simulated annealing method is used to explore the energy landscape and locate low-energy structures. A Monte Carlo sweep consists of two stages: (*i*) an attempt to displace each vertex by a vector $\Delta\vec{r}$ with components chosen at random from a uniform distribution in an interval $[-0.05\ell, 0.05\ell]$ followed by (*ii*) attempts to swap the type of a pair of randomly selected vertices. Moves in both stages are accepted or rejected according to Metropolis rules. The type-swap move is introduced to allow for a simultaneous optimization of the component arrangement and the shell shape. Although the obtained structures inevitably depend on the cooling protocol used, the lowest-energy states were obtained by using an exponential cooling profile for vertex displacements and a linear profile for type swapping. In a typical simulation, an optimal configuration was reached after 1.2×10^6 sweeps. Multiple runs with the same relative fraction but different initial random distributions of the components were used to ensure that the obtained low-energy structures were qualitatively reproducible.

Microscopy. The images in Fig. 2 *A* and *B* are nuclei from HeLa cells with lamin B1 silencing, and thus, only A-type lamins and lamin B2 are labeled. The preparation and immunofluorescence methods used to produce these images are detailed by Shimi et al. (16), the study from which Fig. 2*A* is reproduced. Figs. 1*A* and 2*C* present nuclei from breast cancer cell line MDAMB231, with similar immunofluorescence labeling as the images in Fig. 2 *A* and *B*. Lastly, the nuclei imaged in Fig. 2*E* are from fibroblasts of a male progeria patient with the E145K-LA mutation, with the materials and methods detailed by Taimen et al. (61).

ACKNOWLEDGMENTS. We thank John F. Marko and Stephen A. Adam for helpful discussions during development of the model and Pekka Taimen for the progeria cell nucleus images. Numerical simulations were performed using the Northwestern University High Performance Computing Cluster Quest. C.M.F. and M.O.d.l.C. were funded by the Office of the Director of Defense Research and Engineering (DDR&E) and Air Force Office of Scientific Research (AFOSR) Award FA9550-10-1-0167. R.S. and M.O.d.l.C. acknowledge the financial support of US Department of Energy Award DEFG02-08ER46539. R.D.G. is supported by National Cancer Institute Grant 5R01 CA031760-28 and the Progeria Research Foundation.

1. Dahl KN, Kahn SM, Wilson KL, Discher DE (2004) The nuclear envelope lamina network has elasticity and a compressibility limit suggestive of a molecular shock absorber. *J Cell Sci* 117(Pt 20):4779–4786.
2. Rowat AC, Foster LJ, Nielsen MM, Weiss M, Ipsen JH (2005) Characterization of the elastic properties of the nuclear envelope. *J R Soc Interface* 2(2):63–69.
3. Lammerding J, et al. (2006) Lamins A and C but not lamin B1 regulate nuclear mechanics. *J Biol Chem* 281(35):25768–25780.
4. Stuurman N, Heins S, Aebi U (1998) Nuclear lamins: Their structure, assembly, and interactions. *J Struct Biol* 122(1-2):42–66.
5. Goldman RD, Gruenbaum Y, Moir RD, Shumaker DK, Spann TP (2002) Nuclear lamins: Building blocks of nuclear architecture. *Genes Dev* 16(5):533–547.
6. Dechat T, et al. (2008) Nuclear lamins: Major factors in the structural organization and function of the nucleus and chromatin. *Genes Dev* 22(7):832–853.
7. Mounkes L, Kozlov S, Burke B, Stewart CL (2003) The laminopathies: Nuclear structure meets disease. *Curr Opin Genet Dev* 13(3):223–230.
8. Capell BC, Collins FS (2006) Human laminopathies: Nuclei gone genetically awry. *Nat Rev Genet* 7(12):940–952.
9. Maraldi NM, et al. (2006) Laminopathies: A chromatin affair. *Adv Enzyme Regul* 46 (2006):33–49.
10. Zink D, Fischer AH, Nickerson JA (2004) Nuclear structure in cancer cells. *Nat Rev Cancer* 4(9):677–687.
11. Goldman RD, et al. (2004) Accumulation of mutant lamin A causes progressive changes in nuclear architecture in Hutchinson-Gilford progeria syndrome. *Proc Natl Acad Sci USA* 101(24):8963–8968.
12. Vigouroux C, et al. (2001) Nuclear envelope disorganization in fibroblasts from lipodystrophic patients with heterozygous R482Q/W mutations in the lamin A/C gene. *J Cell Sci* 114(Pt 24):4459–4468.

13. Novelli G, et al. (2002) Mandibuloacral dysplasia is caused by a mutation in LMNA-encoding lamin A/C. *Am J Hum Genet* 71(2):426–431.
14. Caux F, et al. (2003) A new clinical condition linked to a novel mutation in lamins A and C with generalized lipoatrophy, insulin-resistant diabetes, disseminated leukomelanodermic papules, liver steatosis, and cardiomyopathy. *J Clin Endocrinol Metab* 88(3):1006–1013.
15. Muchir A, et al. (2004) Nuclear envelope alterations in fibroblasts from patients with muscular dystrophy, cardiomyopathy, and partial lipodystrophy carrying lamin A/C gene mutations. *Muscle Nerve* 30(4):444–450.
16. Shimi T, et al. (2008) The A- and B-type nuclear lamin networks: Microdomains involved in chromatin organization and transcription. *Genes Dev* 22(24):3409–3421.
17. Rowat AC, Lammerding J, Herrmann H, Aebi U (2008) Towards an integrated understanding of the structure and mechanics of the cell nucleus. *Bioessays* 30(3):226–236.
18. Guilak F, Tedrow JR, Burgkart R (2000) Viscoelastic properties of the cell nucleus. *Biochem Biophys Res Commun* 269(3):781–786.
19. Schäpe J, Prausse S, Radmacher M, Stick R (2009) Influence of lamin A on the mechanical properties of amphibian oocyte nuclei measured by atomic force microscopy. *Biophys J* 96(10):4319–4325.
20. Vaziri A, Lee H, Kaazempur Mofrad MR (2006) Deformation of the cell nucleus under indentation: Mechanics and mechanisms. *J Mater Res* 21(8):2126–2135.
21. Qin Z, Buehler MJ (2011) Flaw tolerance of nuclear intermediate filament lamina under extreme mechanical deformation. *ACS Nano* 5(4):3034–3042.
22. Wren NS, Zhong Z, Schwartz RS, Dahl KN (2012) Modeling nuclear blebs in a nucleoskeleton of independent filament networks. *Cell Mol Bioeng* 5(1):73–81.
23. Vernizzi G, Sknepnek R, Olvera de la Cruz M (2011) Platonic and Archimedean geometries in multicomponent elastic membranes. *Proc Natl Acad Sci USA* 108(11):4292–4296.
24. Norman LL, Brugués J, Sengupta K, Sens P, Aranda-Espinoza H (2010) Cell blebbing and membrane area homeostasis in spreading and retracting cells. *Biophys J* 99(6):1726–1733.
25. Aebi U, Cohn J, Buhle L, Gerace L (1986) The nuclear lamina is a meshwork of intermediate-type filaments. *Nature* 323(6088):560–564.
26. Goldberg MW, Huttenlauch I, Hutchison CJ, Stick R (2008) Filaments made from A- and B-type lamins differ in structure and organization. *J Cell Sci* 121(Pt 2):215–225.
27. Dahl KN, et al. (2006) Distinct structural and mechanical properties of the nuclear lamina in Hutchinson-Gilford progeria syndrome. *Proc Natl Acad Sci USA* 103(27):10271–10276.
28. Fawcett DW (1966) On the occurrence of a fibrous lamina on the inner aspect of the nuclear envelope in certain cells of vertebrates. *Am J Anat* 119(1):129–145.
29. Senda T, Iizuka-Kogo A, Shimomura A (2005) Visualization of the nuclear lamina in mouse anterior pituitary cells and immunocytochemical detection of lamin A/C by quick-freeze freeze-substitution electron microscopy. *J Histochem Cytochem* 53(4):497–507.
30. Höger TH, Grund C, Franke WW, Krohne G (1991) Immunolocalization of lamins in the thick nuclear lamina of human synovial cells. *Eur J Cell Biol* 54(1):150–156.
31. Broers JL, et al. (1999) Dynamics of the nuclear lamina as monitored by GFP-tagged A-type lamins. *J Cell Sci* 112(Pt 20):3463–3475.
32. Moir RD, Yoon M, Khuon S, Goldman RD (2000) Nuclear lamins A and B1: Different pathways of assembly during nuclear envelope formation in living cells. *J Cell Biol* 151(6):1155–1168.
33. Panorchan P, Schafer BW, Wirtz D, Tseng Y (2004) Nuclear envelope breakdown requires overcoming the mechanical integrity of the nuclear lamina. *J Biol Chem* 279(42):43462–43467.
34. Dahl KN, Engler AJ, Pajerowski JD, Discher DE (2005) Power-law rheology of isolated nuclei with deformation mapping of nuclear substructures. *Biophys J* 89(4):2855–2864.
35. Koiter WT (1966) On the nonlinear theory of thin elastic shells. *Proc K Ned Akad Wet B* 69(1):1–54.
36. Seung HS, Nelson DR (1988) Defects in flexible membranes with crystalline order. *Phys Rev A* 38(2):1005–1018.
37. Efrati E, Sharon E, Kupferman R (2009) Elastic theory of unconstrained non-Euclidean plates. *J Mech Phys Solids* 57(4):762–775.
38. Landau LD, Lifshitz EM (1995) *Theory of Elasticity* (Butterworth-Heinemann, Boston), 3rd Revised Ed.
39. Sknepnek R, Olvera de la Cruz M (2012) Nonlinear elastic model for faceting of vesicles with soft grain boundaries. *Phys Rev E Stat Nonlin Soft Matter Phys* 85(5 Pt 1):050501.
40. Huang J, Liu J, Kroll B, Bertoldi K, Clarke DR (2012) Spontaneous and deterministic three-dimensional curling of pre-strained elastomeric bi-strips. *Soft Matter* 8(23):6291–6300.
41. Sharon E, Roman B, Marder M, Shin GS, Swinney HL (2002) Mechanics. Buckling cascades in free sheets. *Nature* 419(6907):579–579.
42. Marder M, Sharon E, Smith S, Roman B (2003) Theory of edges of leaves. *Europhys Lett* 62(4):498–504.
43. Audoly B, Boudaoud A (2003) Self-similar structures near boundaries in strained systems. *Phys Rev Lett* 91(8):086105.
44. Sharon E, Efrati E (2010) The mechanics of non-Euclidean plates. *Soft Matter* 6(22):5693–5704.
45. Datta SS, et al. (2012) Delayed buckling and guided folding of inhomogeneous capsules. *Phys Rev Lett* 109(13):134302.
46. Razafsky D, Hodzic D (2009) Bringing KASH under the SUN: The many faces of nucleo-cytoskeletal connections. *J Cell Biol* 186(4):461–472.
47. Zhong Z, Wilson KL, Dahl KN (2010) *Beyond Lamins: Other Structural Components of the Nucleoskeleton*, ed Shivashankar GV (Academic, London), Vol 98, pp 97–119.
48. Shimi T, Butin-Israeli V, Goldman RD (2012) The functions of the nuclear envelope in mediating the molecular crosstalk between the nucleus and the cytoplasm. *Curr Opin Cell Biol* 24(1):71–78.
49. Chen CY, et al. (2012) Accumulation of the inner nuclear envelope protein Sun1 is pathogenic in progeric and dystrophic laminopathies. *Cell* 149(3):565–577.
50. Sknepnek R, Vernizzi G, Olvera de la Cruz M (2012) Buckling of multicomponent elastic shells with line tension. *Soft Matter* 8(3):636–644.
51. Audoly B, Pomeau Y (2010) *Elasticity and Geometry—From Hair Curls to the Non-Linear Response of Shells* (Oxford Univ Press, Oxford).
52. Green AE, Zerna W (2002) *Theoretical Elasticity* (Dover, New York).
53. Weeks JD, Chandler D, Andersen HC (1971) Role of repulsive forces in determining the equilibrium structure of simple liquids. *J Chem Phys* 54(12):5237–5247.
54. Renka RJ (1997) Algorithm 772: STRIPACK: Delaunay triangulation and Voronoi diagram on the surface of a sphere. *ACM Trans Math Softw* 23(3):416–434.
55. Katifori E, Alben S, Cerda E, Nelson DR, Dumais J (2010) Foldable structures and the natural design of pollen grains. *Proc Natl Acad Sci USA* 107(17):7635–7639.
56. Nelson DR, Piran T, Weinberg S (2004) *Statistical Mechanics of Membranes and Surfaces* (World Scientific, STeaneck, NJ), 2nd Ed.
57. Magid E, Soldea O, Rivlin E (2007) A comparison of Gaussian and mean curvature estimation methods on triangular meshes of range image data. *Comput Vis Image Underst* 107(3):139–159.
58. Gompper G, Kroll DM (1996) Random surface discretizations and the renormalization of the bending rigidity. *J Phys I* 6(10):1305–1320.
59. Sunil Kumar PB, Gompper G, Lipowsky R (2001) Budding dynamics of multicomponent membranes. *Phys Rev Lett* 86(17):3911–3914.
60. Itzykson C (1986) *Random Geometry, Lattices and Fields*, eds Abad J, et al. (World Scientific, Singapore), pp 130–188.
61. Taimen P, et al. (2009) A progeria mutation reveals functions for lamin A in nuclear assembly, architecture, and chromosome organization. *Proc Natl Acad Sci USA* 106(49):20788–20793.

APPLIED PHYSICAL SCIENCES